SAND2015-10813C

# Relationship between Transonic Cavity Tones and Flowfield Dynamics using Pulse-Burst PIV

Justin L. Wagner,[1] Steven J. Beresh,[2] Katya M. Casper[3], Edward P. DeMauro,[4] Srinivasan Arunajatesan,[5]
John F. Henfling,[6] and Russell W. Spillers[7]
*Sandia National Laboratories, Albuquerque, NM, 87185*

**Mach 0.94 flow over a cavity having a length-to-depth ratio of five was explored using time-resolved particle image velocimetry (TR-PIV) with a burst-mode laser. Convective velocities were computed using cross correlations. The convective velocity measured in the shear layer increased with streamwise distance in a fashion similar to other studies. The TR-PIV data were used to probe the resonance dynamics of the first three cavity (Rossiter) tones. Bandpass filtering was employed to reveal the coherent flow structure associated with each tone. The first Rossiter mode was associated with a propagation of large scale structures in the recirculation region, while the second and third modes contained organized structures consistent with convecting vortical disturbances. The wavelengths of the second and third modes were quite similar to those observed in a previous study by the current authors using phase averaged PIV. Convective velocities of the cavity tones were found to decrease with mode number, consistent with the modal activity residing in lower portions of the cavity in regions of lower local mean velocities. The convective velocity fields were found to have wavelengths that decreased with increasing mode number. Such oscillations were hypothesized to be associated with wall-normal motions of coherent structures during resonance.**

## I. Introduction

The flow over an open cavity generates large pressure fluctuations associated with broadband turbulence and cavity resonance [1], which can result in high levels of structural vibrations [2-5]. Since cavity flow is analogous in many ways to an open aircraft bay in flight, the subject has received much attention over the last sixty plus years as detailed in the review articles of Rockwell and Naudascher [6, 7], Rowley and Williams [8], and Cattafesta et al. [9]. In subsonic flows, when the cavity length-to-depth ratio $L/D$ is less than about seven [10], an interaction of the cavity's acoustic field and free shear layer form a feedback loop that results in resonant oscillations [1]. The resonant modes are primarily longitudinal and in rectangular geometries, the tonal frequencies are reasonably predicted by the semi-empirical relation provided in the seminal work of Rossiter [1].

In comparison to modal frequencies, prediction of the modal amplitudes is much more difficult as the pressure magnitudes are sensitive functions of the flow conditions (boundary layer properties, Mach number, e.g.) as well as the cavity geometry ($L/D$, length-to-width ratio $L/W$, e.g.) [10]. Changes to geometric parameters such as $L/W$ also lead to modifications of cavity turbulence levels [11 - 13], which is expected to alter the overall broadband loading.

---

[1] Senior Member of the Technical Staff, Engineering Sciences Center, P.O. Box 5800, Mailstop 0825; jwagner@sandia.gov. AIAA Senior Member.
[2] Distinguished Member of the Technical Staff, Engineering Sciences Center, AIAA Associate Fellow.
[3] Senior Member of the Technical Staff, Engineering Sciences Center, AIAA Senior Member.
[4] Post-doctoral Appointee, Engineering Sciences Center, AIAA Member.
[5] Principal Member of the Technical Staff, Engineering Sciences Center, AIAA Senior Member.
[6] Distinguished Technologist, Engineering Sciences Center, AIAA Member.
[7] Principal Technologist, Engineering Sciences Center.
[8] Senior Technologist, Engineering Sciences Center.

This work is supported by Sandia National Laboratories and the United States Department of Energy. Sandia National Laboratories is a multi-program laboratory managed and operated by Sandia Corporation, a wholly owned subsidiary of Lockheed Martin Corporation, for the U.S. Department of Energy's National Nuclear Security Administration under contract DE-AC04-94AL85000

Furthermore, geometric complexities associated with real weapons bays, such as inflow ramps and doors can create enhanced resonance conditions [14] with complicated, three-dimensional flow features [15, 16].

Other challenges lie in understanding the temporal behavior of resonating cavity flows. Cavity flow dynamics involve a complex interaction of separated/recirculating flow, turbulence and aeroacoustic resonance. Additionally, although a given cavity flow can be associated with several tonal frequencies, the tones do not necessarily occur simultaneously. Rather the dominant cavity mode can vary with time – a process known as 'mode-switching'. The idea for mode switching was first proposed in the earlier works of Krishnamurty [17] and Sarohia [18], later proven in the experiments of Kegerise et al. [19, 20], and observed in the simulations of Larchevêque et al. [21] shortly thereafter. Fairly recent simulations by Brès and Colonious [22] suggested that spanwise instabilities can lead to low-frequency modulations of Rossiter modes, a result perhaps consistent with the low-frequency spanwise modulations of the cavity pressure field later observed using modal analysis in Casper and Arunajatesan [23]. An additional, unique view on cavity dynamics is given by Delprat who theorizes that cavity modes are not unique, rather they are modulations of a fundamental loop frequency $f_a$, which is equal to the difference between any cavity tone $f_n$ and the next lowest cavity tone frequency $f_{n-1}$ (i.e., $f_n - f_{n-1}$). Furthermore, Delprat suggests low frequency modulation of a cavity tone can be simply predicted using the phase delay constant $\alpha$ in Rossiter's equation. Despite these examples of recent progress, the dynamics of cavity flows, particularly in the high-speed regime, is an evolving research area. A common consensus on the physical mechanisms of cavity tone modulations has not been reached.

Experimental data capturing cavity flowfield dynamics are required to develop and validate new theoretical models. In compressible flows, however, measurements techniques to do so, such as particle image velocimetry (PIV), are usually made at repetition rates far too low to capture dynamics in a truly time-resolved fashion. To overcome this, stochastic estimation methods have been used to create low-dimensional representations of the velocity field informed by time-resolved pressure data [24, 25]. Such methods have been used to track the effect of resonant flow structures on surface pressures [24]. In another example, Murray et al. [25] used stochastic methods to show that Rossiter pressure fluctuations were primarily influenced by mean-shear velocity terms in Poisson's equation as opposed to non-linear, turbulent velocity fluctuation terms.

An alternative method to measure transonic cavity resonance dynamics using low repetition rate PIV and simultaneous high-speed pressure data was recently developed by the current authors [26]. In short, the pressure data were bandpass filtered about the cavity tone frequencies using joint-time frequency analysis and used to conditionally average the PIV data. Triple-decomposition [27] then revealed the flow structure associated with cavity resonant tones. The first Rossiter mode was associated with large scale oscillations in the shear layer and recirculation region, while the second and third modes contained organized structures seemingly consistent with convecting vortical disturbances. The spacing between coherent structures suggested the convective velocity of downstream-propagating disturbances was less than that typically used in the Rossiter relation.

Time-resolved PIV measurements were also made in [26] using a burst-mode laser. Preliminary analysis on a subset of the time-resolved data was performed by bandpass filtering the time-resolved velocity data about the cavity tone frequencies. Like the phase averaged results, the time-resolved convective velocities were lower than those typically used in the Rossiter relation. Furthermore, initial analysis suggested that the convective velocity was found to be dependent on cavity mode number.

The current work extends analysis of the burst-mode PIV data to further elucidate transonic cavity dynamics during resonance. Bandpass filtered sequences of velocity vector fields are used to highlight the coherent flow structures observed during resonance. Quantitative comparisons to previous coherent structures are then made using the previous phase averaged flowfields. Finally, two-point correlations of the velocity field reveal how convective velocity varies across the length and height of the cavity for the first three cavity modes while spectral analysis is used to explain these variations.

## II. Experimental Program

### A. Trisonic Wind Tunnel (TWT)

Experiments were conducted in the blowdown-to-atmosphere TWT. The facility uses air as the test gas and has a test section enclosed in a pressurized plenum. During a run, the stagnation temperature $T_0$ was held constant at about 321 K. Data were obtained at freestream Mach numbers $M_\infty$ of 0.60, 0.80, and 0.94, where the Mach number was determined using freestream velocity measurements at the cavity entrance location and the assumption of isentropic expansion. About sixty wind tunnel runs per made per condition. As discussed subsequently, the Mach 0.94 flow had three active cavity tones making it an ideal case for the current work. Thus, the focus here is at this Mach number. Typical flow conditions for the experiments conducted in the 305 × 305 mm$^2$ test section are given in Table 1. The freestream dynamic pressure $q_\infty$ was held constant to about 33 kPa. The tunnel wall boundary layers developed naturally and were fully turbulent upon arrival at the test section. Previous measurements have indicated that the 99% wall boundary layer thickness at the cavity entrance is about 13 mm or about half the cavity depth.

**Table 1: Typical TWT Experimental Conditions**

| $M_\infty$ | $P_0$, kPa | Re × $10^{-6}$, /m |
|---|---|---|
| 0.94 | 60 | 13 |

In subsonic cavity flows it is necessary to mitigate the undesirable acoustical interference associated with solid wind tunnel walls by placing an acoustic absorber in the wall opposite to the cavity [19, 28-29]. As described in a recent study by the current authors, the spanwise walls of subsonic test sections can also lead to acoustical contamination if untreated [30]. To reduce these effects, the wall opposite the cavity and one spanwise wall were replaced with acoustic dampeners, which consisted of a porous wall (used typically for transonic testing) backed by acoustical absorption foam. The opposite spanwise wall was solid with a window providing a view for the PIV cameras.

## B. Cavity

The cavity had length $L$ of 127 mm, width $W$ of 127 mm, and depth $D$ of 25.4 mm and was installed in the lower wall of the test section (Fig. 1). With an $L/D$ of 5, the cavity flow category is 'open' and expected to resonate [10]. The streamwise (x), wall-normal (y), spanwise (z) coordinate system originates at the spanwise center of the cavity leading edge. The wind tunnel floor is defined to be at $y = 0$, with positive $y$ pointing away from cavity.

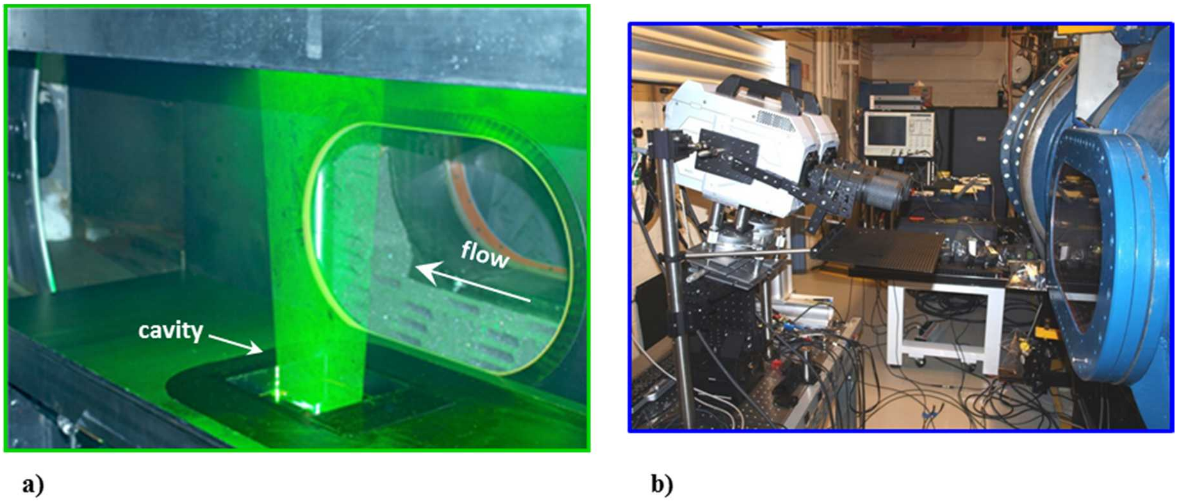

**Fig. 1 Cavity and PIV setup photos: (a) cavity in the lower wall of the test section and the PIV laser sheet [30], and (b) Photron SA-Z cameras at a downward angle to image one half of the cavity depth**

## C. Unsteady Pressures

Measurement Details

Eight dynamic pressure sensors (Kulite XCQ-062-30A or similar) having a range of about 207 kPa and a flat frequency response up until about 50 kHz were placed in the cavity fore-wall and aft-wall. The sensors were located along the span of these walls, though only data at $z = 0$ is used for analysis here. The sampling frequency was 200 kHz and the data were low-pass-filtered at 50 kHz. Previous experiments have confirmed that the cavity pressures scale with $q_\infty$ and that the data are highly repeatable [2].

Analysis Methods

Power spectral density (PSD) spectra are shown herein, which were generated using a total of at least 2 million samples and were computed using the Welch windowing algorithm in the Mathworks software package (MatLab R2013b). Blackman windows with an overlap of 50% and a window length of 10 Hz were used for the spectra.

Joint-time frequency analysis (JTFA) of the pressure traces was conducted using a wavelet transform. This technique shows the frequency content of the disturbances as a function of time, and has been used in other unsteady applications such as wake transition, meteorological studies, and cavity flows [20, 31-33]. The transform provides good time resolution for identifying intermittent mode switching within the cavity. However, it has poor frequency resolution compared to alternate joint time-frequency methods such as the short-time-Fourier transform. The wavelet transform was computed using a Mathworks (Matlab) script provided in Ref. [33]. A Morelet mother wavelet was chosen.

### D. Pulse-Burst PIV

Measurement Details

Seeding was provided by a smoke generator (Corona Vi-Count 5000) that produced a large quantity of mineral oil particles. Particles were delivered to the tunnel stagnation chamber upstream of the flow conditioning section. Measurement of the *in-situ* particle response across a shock wave generated by a wedge has shown the particle size to be about 0.8 µm. Stokes numbers are estimated to be about 0.04 based on *a posteriori* measurements of typical cavity shear layer eddies. Thus, the particles rapidly attain the local velocity even in the presence of velocity gradients in the shear layer [34]. Inspection of the PIV images showed adequate seeding in all portions of the cavity, including the recirculation region.

A quasi-continuous burst-mode laser (QuasiModo-1000, Spectral Energies, LLC) with both diode and flashlamp Nd:YAG amplifiers was used to produce a high energy pulse train at 532 nm in a separate set of experiments. The design of the pulse-burst laser is based on master oscillator power amplifier architecture and is similar to previously reported pulse-burst lasers [35-36]. As detailed in [37], the laser is capable of producing doublets with variable inter-pulse spacing and pulse frequencies. Here, 37.5 kHz doublets separated by 3 µs were used. The pulse-burst laser generated a 10.2 ms burst every 8 seconds and the energy per pulse was about 30 mJ. Five bursts per run were obtained bringing the total number of independent bursts (time series) per condition to three hundred. The beam from the pulse-burst laser was shaped into a laser sheet covering the streamwise length of the cavity and with a spanwise thickness of about 1.5 mm. The sheet was located at the spanwise center of the cavity.

Images were acquired using two high-speed CMOS cameras (Photron SA-Z). Each camera was operated at 75 kHz with a resolution of 640 × 384 pixels. The two pulses in a doublet were frame-straddled around the interframe transfer time of the cameras to produces separate images for cross-correlation analysis. As a result, the PIV repetition rate was half that of the framing-rate, or 37.5 kHz.

The two cameras were placed side-by-side as shown in Fig. 1b to extend the field of view in the streamwise direction. The resulting combined field-of-view was about 120 × 30 mm. As detailed in Beresh et al. [11], PIV measurements for rectangular cavities in the TWT have limited optical access due to the presence of the pressurized plenum that surrounds the test section. Moreover, since the cavities are three-dimensional, solid walls obstruct a direct view of a submerged cavity cutout. To overcome this, the cameras were also angled vertically downward by about 12 degrees to view inside the cavity directly in this case without a mirror. As a result, the cameras imaged about 50% of the cavity depth in contrast to the 100% in the previous 10-Hz data [26]. Such an angle is expected to bias the vertical velocities by about 20%, though previous experience has shown that this bias does not prevent the visualization of turbulent structures [11].

About 120,000 vector fields were acquired at each Mach number. However, the since the fields within a burst were correlated in time, the number of independent sets of vector fields corresponds to the total number of burst used per Mach number, namely three hundred. Processing was performed using the LaVision (DaVis 8.2) software package. Image pairs were interrogated with an initial pass using 64 × 64 pixel interrogation windows, followed by two iterations of 24 × 24 pixel interrogation windows, incorporating adaptive window offsets and image deformation based upon local velocity gradients. A 50% overlap in the interrogation windows was used. The resulting vector fields were validated based upon signal-to-noise ratio, nearest-neighbor comparisons, and allowable velocity range. To better reveal coherent flow structures, the vector fields were lightly smoothed with a low-pass filter.

Analysis Methods

Velocity PSDs were computed at each vector location in a manner similar to the pressure spectra. Blackman windows with an overlap of 50% and a window length of about 100 Hz were used for the spectra. A finer frequency resolution for the velocity spectra was not possible owing to the limited 10.2 ms time of each burst. Spatial distributions of the PSD amplitude at frequencies corresponding to cavity tones are presented herein to highlight the most active regions associated with cavity resonance in a manner similar to that in [37].

The velocity fields were bandpass filtered in the time domain about each of the cavity tone frequencies. A Butterworth filter based on the algorithm in Russell [38] was used. This algorithm uses a cascade of first order filters instead of quadratic filters and hence is very precise for narrow band applications such as the present one. Furthermore, the data are forward and backward filtered to produce zero phase shift. The code provided in Ref. [38] was used in the present work. Filtering the pressure data with this same filtering method showed the filter results in very little signal attenuation at the desired frequency band.

Cross correlations between velocity time sequences at points separated at fixed streamwise distance were computed allowing for the streamwise convection velocity between the points to be calculated. Additional details on the cross correlation analysis is detailed in the results.

## III. Results

### A. Mean Flow

The mean flowfield over nearly the entire height and length of the cavity obtained from previous PIV measurements [12, 26] is shown in Fig. 2a. The flow demonstrates the expected behavior of a mixing layer that grows with streamwise distance. A single recirculation region centered at about $x/D = 3.4$ is also evident. Below the cavity lip line ($y = 0$), the flow is turned downward in the mixing layer to impinge on the aft-wall. In contrast, the sample instantaneous flowfield shown in Fig. 2b shows the mixing layer to be undulated. Three vortical like structures (A, B, and C) are observed within the cavity. The purpose of this work is to understand the dynamics of such flow structures associated with a given cavity tone.

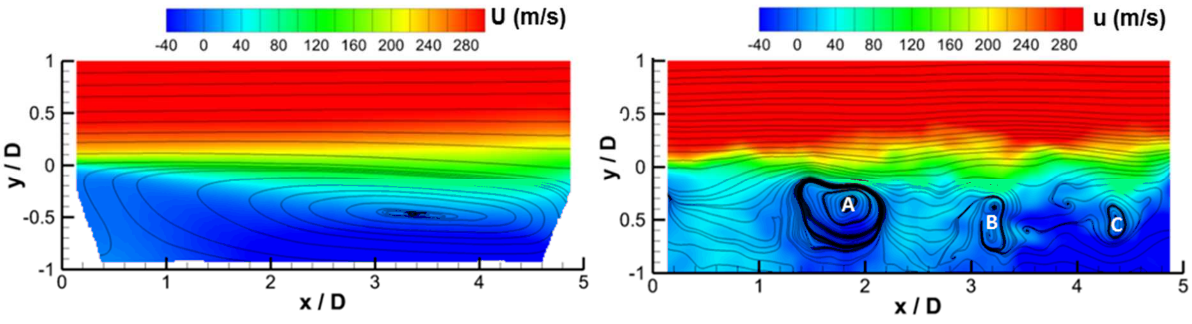

a) b)

**Fig. 2 Mach 0.94 PIV : (a) mean streamwise flow velocity U contours with superposed streamlines, and (b) instantaneous streamwise velocities *u* with superposed streamlines.**

### B. Cavity Pressure Spectra

*SPL* spectra obtained at the fore-wall and aft-wall of the cavity are shown in Fig. 3, for the freestream Mach number of 0.94. In this case, the amplitudes of the first three Rossiter modes are quite similar and reside within a few dB of one another. A fourth cavity tone is also observed. The expected frequencies of the cavity tones can be given with the Rossiter relation modified for compressible flows of Heller and Bliss [39]:

$$St = \frac{f_m L}{U_\infty} = \frac{m - \alpha}{\left[ M_\infty \left(1 + \frac{\gamma - 1}{2} M_\infty\right)^{-1/2} + \frac{1}{\kappa} \right]} \qquad (1)$$

where $f$ is frequency, $m$ is integer mode number, $U_\infty$ is freestream velocity, and $\gamma$ is the ratio of specific heats. This semi-empirical equation is based on the assumption that vortical disturbances associated with resonance propagate downstream at a constant convection velocity of $\kappa \times U_\infty$. When a disturbance reaches the aft-wall, there is a phase lag $\alpha$ (in fractions of a wavelength), which occurs before an upstream-propagating disturbance is formed. The upstream-propagating disturbance then moves at the stagnation speed of sound. Throughout the literature, commonly used constants for phase lag and convective velocity are 0.25 and 0.57, respectively [10, 29]. Although the semi-empirical relation is a simplification of the cavity resonance physics, it often provides good predictions of cavity tone frequencies. The current work is no exception. As listed in Table 2 and shown in Fig. 3, using the common values for $\alpha$ and $\kappa$ gives agreement between the measured and predicted frequencies to within 2%.

**Table 2: Measured and Predicted Cavity Tone Frequencies**

| $M_\infty$ | Measured $f_1, f_2, f_3, f_4$ (kHz) | Predicted $f_1, f_2, f_3, f_4$ (kHz) |
|---|---|---|
| 0.94 | 0.69, 1.67, 2.58, 3.50 | 0.70, 1.64, 2.58, 3.51 |

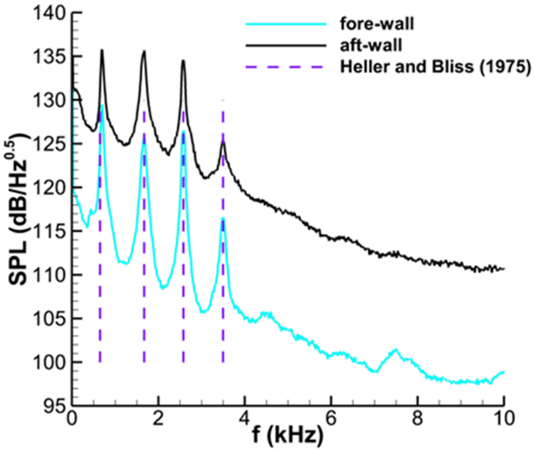

**Fig. 3 Mach 0.94 sound pressure level spectra at the fore-wall and aft-wall of the cavity. M denotes a measured resonance tone. Dashed lines represent frequencies predicted by modified Rossiter relation [39].**

### C. Modulations of Cavity Pressure and Velocity

The dynamic events during cavity flows do not occur uniformly with time. On the contrary, modal amplitudes vary temporally through mode-switching [19-24]. Examples of tonal modulation are shown in Fig. 4, which gives the time varying frequency content of fore-wall pressure measured on two separate runs. Dashed lines appear in the figure to mark the first three cavity modes ($f_1 - f_3$). Though modulated differently, the first cavity mode is fairly active in both subfigures. Modes two and three, however, show substantial differences. For instance, mode two is more active in Fig. 4a, whereas mode three is much more active in Fig. 4b.

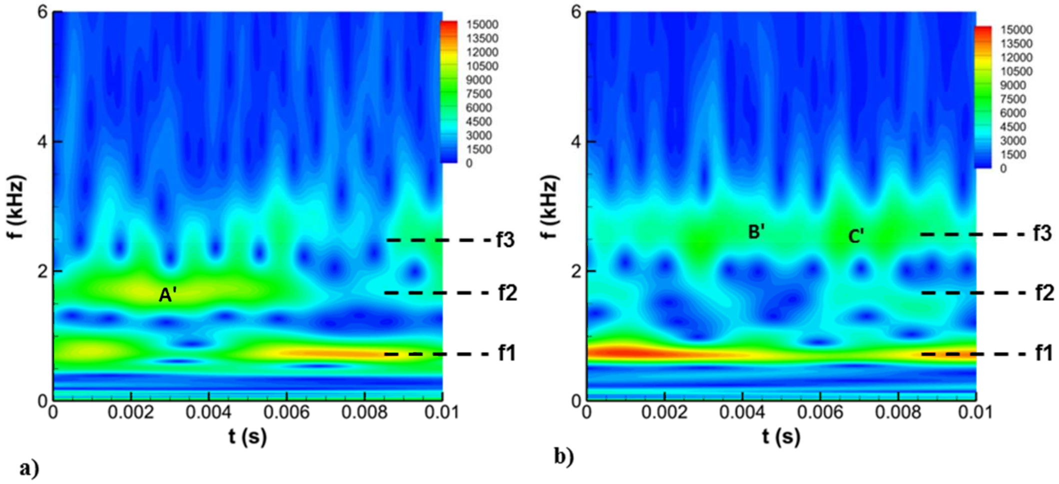

a)

b)

**Fig. 4 Time-frequency content of fore-wall pressure from two separate Mach 0.94 time sequences**

The corresponding variation of frequency content in the velocity data is shown in Fig. 5. The JTFA was performed on the wall-normal velocity *v* at a location of $x = 3.6D$ and $y = 0.1D$ where modes two and three were observed to be quite active in the bandpass filtered *v* fields. The left subfigure corresponds to the same time sequence of Fig. 4a and the right subfigure corresponds to Fig. 4b. Similar to the pressure frequency content, the third cavity tone is observed to be much more active in the right subfigure than in the left. Also, like the pressure data, mode two contains more energy in the left subfigure. In both Fig. 4a and Fig. 5a, mode two exhibits a peak around a time of 0.003 seconds (labels A and A'). Some correlation between Fig. 4b and Fig. 5b can also be seen for third cavity mode (B and C), although it is less pronounced than the subfigures where mode two is more active. The correlation between the pressure and velocity figures at mode one is not as strong, particularly in the left subfigures. This is may be explained by the fact that mode one was most active at lower wall-normal locations, as discussed subsequently.

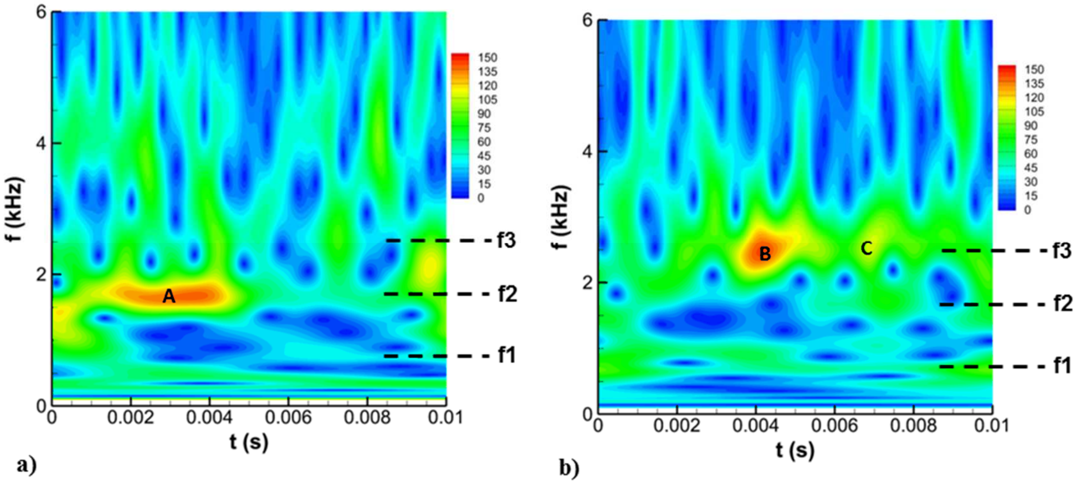

**Fig. 5 Time-frequency content of vertical velocity at $x = 3.6D$ and $y = 0.1D$: (a) same time sequence as Fig. 4a, and (b) same time sequence as Fig. 4b.**

## D. Coherent Structures During Resonance

Although certainly an interesting subject, exploring modulation of cavity tones is not the primary goal of this paper. Rather, the focus here is to investigate the dynamics of cavity tones through bandpass filtering. Since the filtering method employed here is over a narrow band of 100 Hz about each cavity tone, information related to the modulation of cavity tones is not retained since such modulation occurs at much lower frequencies [20-23]. As an example, bandpass filtered velocities of mode two vertical velocity ($v_{f2}$) are shown in Fig. 6. The bandpass filtered velocities were calculated at the same location as in Fig. 5. The high amplitude waveform was calculated from the time sequence when mode two was more active (Fig. 4a and Fig. 5a), whereas the low amplitude waveform corresponds to the less energetic time sequence (Fig. 4b and Fig. 5b). An 'active' mode is defined to occur when the amplitude of the velocity measured at $x = 3.6D$ and $y = 0.1D$ is in the top forty percent in comparison to all the samples. This leaves about one hundred cases of active modes for statistical analysis. A strong periodicity is observed in both signals consistent with the nature narrow frequency band of the filter. Although the bandpass filtering method does not reveal modulation, it is a useful tool to display prominent cavity tone flow structure.

An example is shown in Fig. 7, which gives the bandpass filtered wall-normal velocity $v_{f2}$ (left) and streamwise velocity $u_{f2}$ (right) fields corresponding to a resonant cycle of mode two lasting for a period $T_2$. The filtered sequence was taken from the same time sequence as the high amplitude waveform in Fig. 6. The vertical velocities associated with mode two reveal a clear convection of organized structure as the time increases. At $t = 0$, a region of organized positive vertical velocity appears near $x = D$ (label A). With continuing time, this structure convects downstream reaching a position near $x/D = 3.4$ at $t = 0.87T_2$. Upon completion of a full cycle it is apparent that the upstream region of positive vertical velocity (A) moves downstream to become the larger region of positive vertical velocity (A'). Similar observations are seen in the regions of negative vertical velocities (B and B'). As time progresses from $0.17T_2$ to $0.35T_2$, structure B rises vertically. In contrast, the same structure loses height from times $0.52T_2$ to $0.87T_2$. Interestingly, this vertical motion is occurring in the vicinity of the recirculation region centered at $x = 3.4D$ (Fig. 2a).

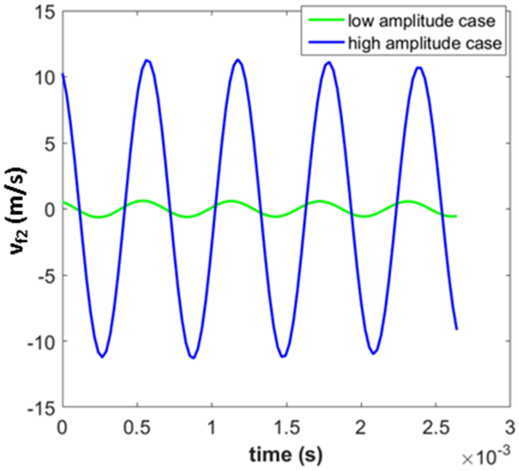

**Fig. 6 Mode two bandpass filtered velocities comparing a low and high amplitude case**

In the streamwise velocity fields regions of positive velocity tend to exist in regions corresponding to negative fluctuations in the vertical fields, indicating a phase shift of about 180 degrees exists between the velocity components. The streamwise coherent velocities exhibit a more complex flow structure than the vertical. A region of negative velocity tends to reside below a region of higher velocity and vice-versa. Furthermore, as the coherent structures propagate from the upstream portion of the cavity to the streamwise center, they also appear to grow diagonally in the upstream direction ($t$ = 0.17$T_2$ and $t$ = 0.70$T_2$). Such behavior does not represent actual convection. Rather, as discussed in Larchevêque et. al [21], it might be related to the fact that the streamwise velocity in cavity flows tends to be more strongly correlated to the pressure waves associated with resonance than the wall-normal velocity. In other words, the apparent upstream growth observed here most likely is related to the propagation of pressure waves and not advection of vortical flow structures. Nevertheless, similar to the wall-normal coherent structures, a convection of negative (C and C') and positive velocities (D and D') is also observed in the streamwise velocities. Additionally, a similar rise (0.17$T_2$ – 0.35$T_2$) and fall (0.52$T_2$ – 0.87$T_2$) of coherent structures in the vicinity of the reticulation region is observed.

A single instance of filtered velocity fields corresponding to the low amplitude waveform in Fig. 6 are shown in Fig. 8. Not surprisingly, the coherent structures are much weaker in comparison to Fig. 7. For this reason, only modes with relatively high amplitudes are used in subsequent cross correlation analysis.

Bandpass filtered velocities corresponding to a mode three cycle with a period $T_3$ are presented in Fig. 9. The figure was generated from the same time sequence as in Fig. 4b and Fig. 5b when mode three was active. Like mode two, an obvious convection of wall normal coherent flow structures is seen with increasing time, though the structures are smaller and more closely spaced, consistent with a lower increase. Once again, the structure of the streamwise coherent velocities is more complex than the wall-normal and regions opposite signed velocity appear under the structures propagating in the shear layer. Also like in mode two, the wall-normal and streamwise fields are roughly 180 degrees out of phase. As the structures propagate downstream they rise upward. A similar upward trajectory of coherent structures has been observed in several incompressible [40, 41], and compressible [42] numerical studies. A possible explanation for this is vortices higher in the shear layer will be less susceptible to being interrupted by the recirculation region. Thus, a structure at a greater $y/D$ may be statistically more likely to remain intact with downstream propagation. The upward motion of the structures does not occur uniformly in the streamwise direction. On the contrary, as depicted with the arrows in the wall-normal velocity subfigures, the most pronounced upward motions occur at $1.5D < x < 2.5D$ ($t$ = 0.64$T_3$, e.g.) and at $3D < x < 4D$ ($t$ = 0.64$T_3$, e.g.). Though difficult to discern in the figures alone, inspection of the corresponding movie (with greater temporal resolution) showed that the wall-normal structures tended to decrease in size while propagating in $2.5D < x < 3D$ and at $x > 4.5D$. The decrease in coherent structure size near the end of the cavity is likely related to the presence of the aft wall and increased turbulence levels. In the case of the streamwise velocities changes the structures also appear to rise more rapidly in over the region $1.5D < x < 2.5D$ ($t$ = 0.64$T_3$, e.g.), although this is more difficult to discern as the structures also grow rapidly in size in this region. Therefore, also similar to mode two, convection of coherent structures is more readily apparent in the wall-normal filtered velocity field than in the streamwise component.

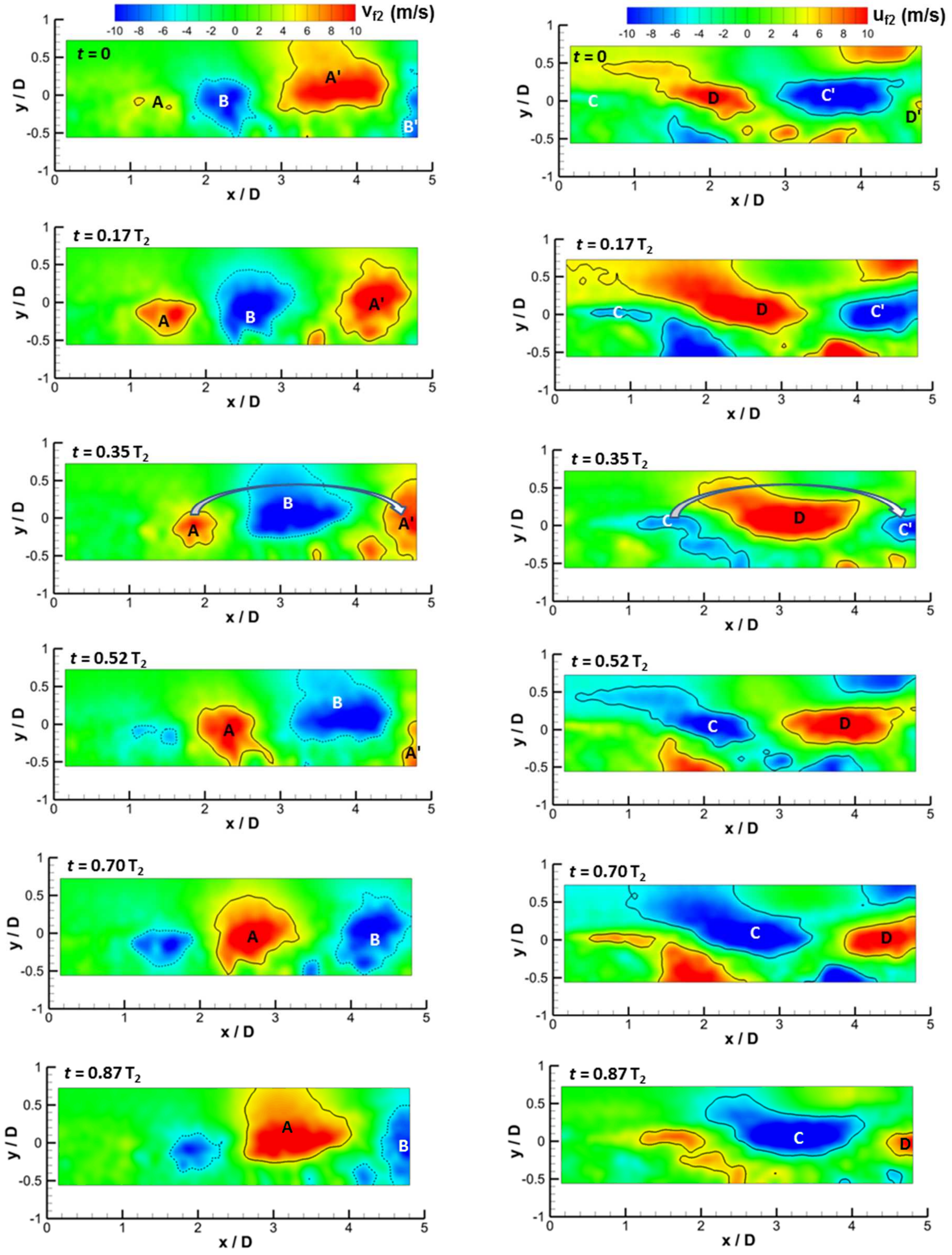

**Fig. 7** ***Mode two*** **bandpass filtered velocities during the high amplitude case: wall-normal (left), and streamwise (right). Solid lines correspond to 5 m/s and dashed lines correspond to -5 m/s.**

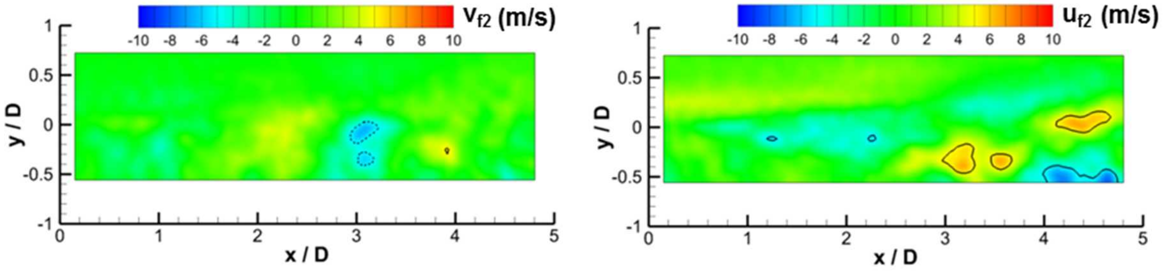

**Fig. 8 Mode two bandpass filtered velocities during the low amplitude case: wall-normal (left), and streamwise (right). Solid lines correspond to 5 m/s and dashed lines correspond to -5 m/s.**

Sample wall-normal coherent flow structures corresponding to modes two and three obtained in the previous study of Wagner et al. [26] are reproduced in Fig. 10 for comparison purposes. The velocity fields shown are the difference of a phase averaged velocity field $V_\theta$ (determined through comparison to bandpassed pressure data) and the mean wall-normal velocity $V$. In Fig. 7, the subfigure at a time of 0.70T$_2$ closely resembles the phase averaged result corresponding to mode two in Fig. 10. In both cases a large region of positive velocity resides near $x = 3D$ and a region of negative velocity is seen near the aft end of the cavity. Similarly, in Fig. 9, the subfigure at a time of 0.86T$_2$ closely resembles the mode three phase averaged result in Fig. 10.

For a quantitative comparison, the velocity fields for these cases were averaged over the wall-normal coordinate to produce the plots shown in Fig. 11. The agreement between the mode two plots is remarkable considering the different methods used to produce the velocity fields. The independent methods also produce reasonable agreement in the mode three plots, although the mode three wavelength corresponding to the pulse-burst data is longer than that in the phase averaged case approaching the aft end of the cavity. For both modes, the wavelength increases with streamwise distance. This would imply that the convective velocity increases with streamwise distance. The variation of convective velocity with cavity position is explored subsequently using the pulse-burst PIV data.

The bandpass filtered velocity fields corresponding to cavity mode one are displayed in Fig. 12. Like modes two and three, a convection of wall-normal flow structure is evident. As time progresses from 0 through the full cycle period T$_1$, the regions of positive (A) and negative (B) wall-normal velocity move downstream. A major difference with respect to the two higher frequency modes is that this convection takes place at a lower wall-normal location. In fact, comparison to the mean flowfield in Fig. 2 suggests that wall-normal coherent structures are moving through a region comprised primarily of the recirculation region.

A convection of flow structure is also seen in the streamwise filtered velocity $u_{f1}$. As time progresses a regions of negative (C) and positive (D) streamwise velocity grow in size and strength while propagating downstream. Similar to modes two and three, the streamwise component is 180 degrees out of phase with the wall-normal. Also similar to the higher order modes is the development of flow structures not consistent with downstream convection. For instance at $t = 0.20$T$_1$, a large region of positive velocity extends from within the recirculation region (C) to the upper half of the cavity including upstream. In the vector fields falling between $t = 0$ and $t = 0.20$T$_1$ the region of positive velocity was observed to grow in the upstream direction while propagating upstream. A similar instance of a large negative velocity region extending from the recirculation region upward through the shear layer and upstream can also be seen at $t = 0.60$T$_1$. Such an observation is likely related to a coupling of the mode one pressure field with the streamwise velocity [21]. In other words, the more reliable indicator of coherent structure convection is given in $v_{f1}$ data.

Many of the preceding observations related to the bandpass filtered velocity fields can be summarized concisely with spatial distributions of PSD amplitude at the given cavity modes. Along these lines, PSD amplitude distributions of wall-normal velocity at frequencies corresponding to cavity tones 1 – 3 are shown in Fig. 13. Full PSDs were generated at each vector location, but only the PSD amplitude at the given cavity tone frequency is shown in the figure. In the case of mode one (Fig. 13a), the PSD peak lies in the recirculation region (Fig. 2a) and most of the energy associated with the mode is contained below $y = 0$ and at $x > 1.5D$, an observation consistent with the location of wall-normal coherent structures shown Fig. 12. As the cavity mode number is increased, the streamwise extent of modal activity grows. This can also be seen in the filtered velocity fields where coherent structures are visible beginning at about $x = D$ at mode two (Fig. 7) and $x = 0.5D$ at mode three (Fig. 9). Furthermore, as the cavity mode number increases from 1 – 3 the mode energy tends to reach higher locations within the flowfield. Finally, the streamwise undulations in PSD amplitude are consistent with locations in the

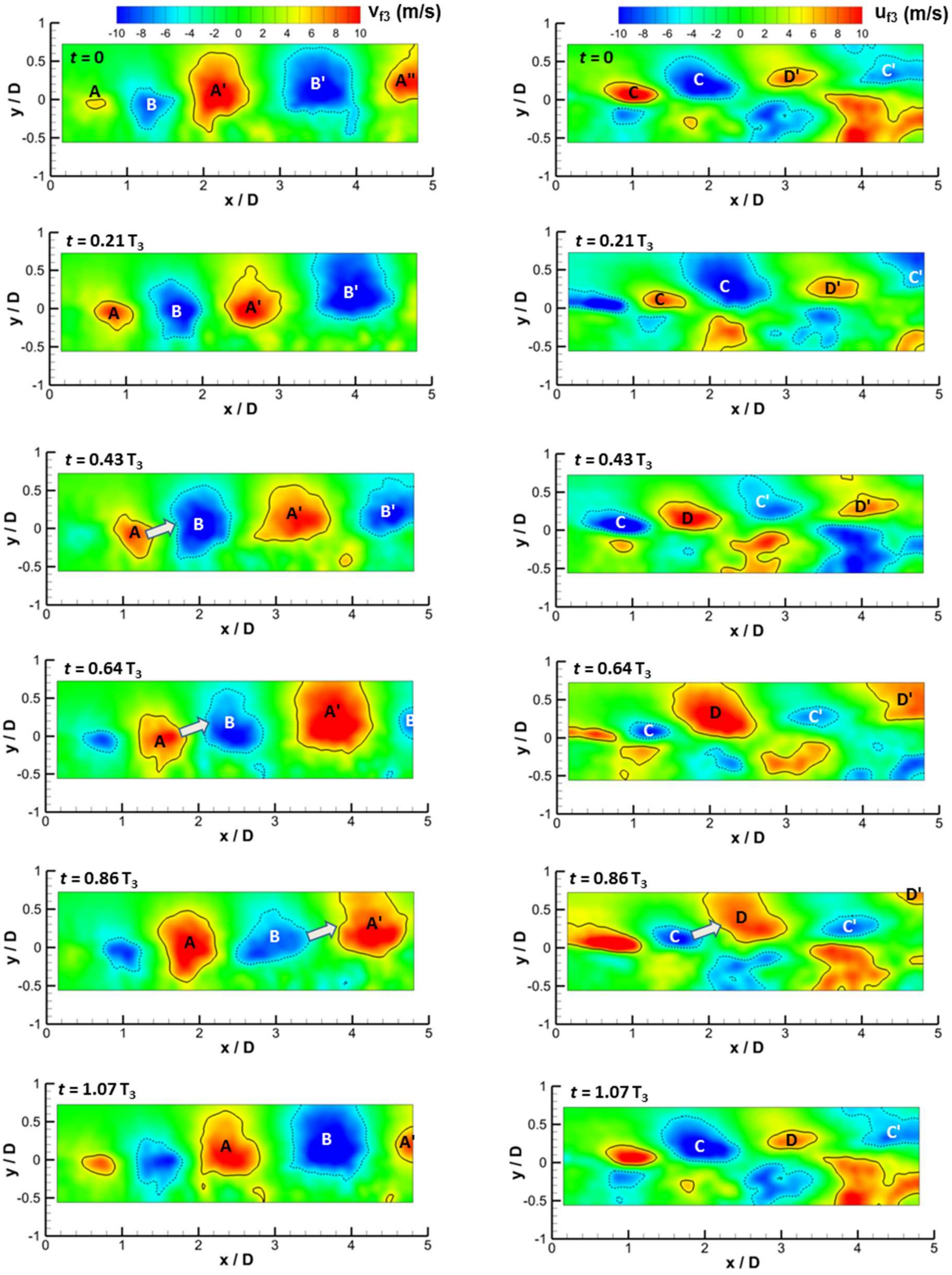

**Fig. 9** ***Mode three*** **bandpass filtered velocities: wall-normal (left), and streamwise (right). Solid lines correspond to 5 m/s and dashed lines correspond to -5 m/s.**

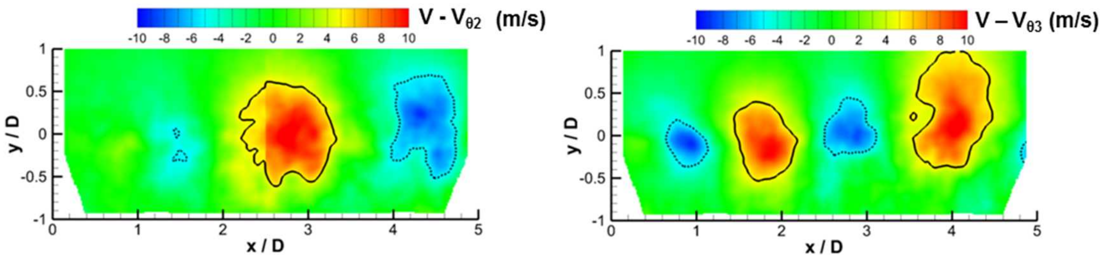

**Fig. 10 Coherent flow structures obtained with phase averaging of low-repetition rate PIV data: (a) *mode two*, and (b) *mode three***

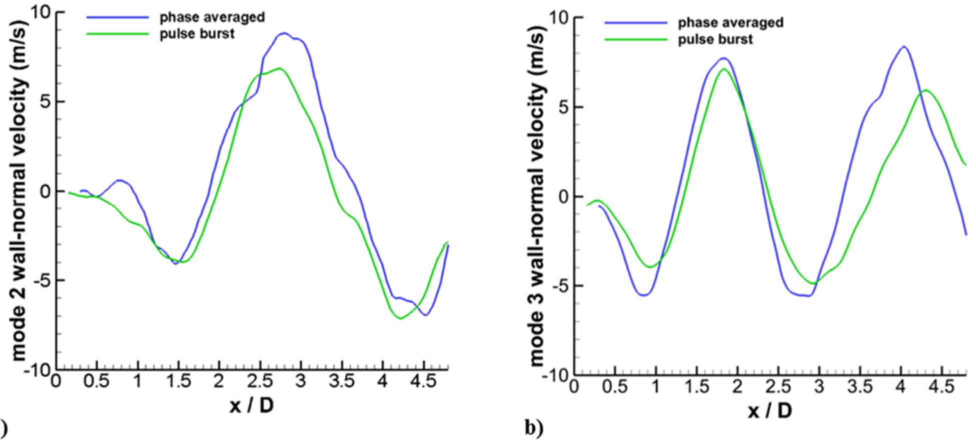

a) b)

**Fig. 11 Wall-normal velocity as a function of *x* corresponding to the bandpass filtered pulse-burst data and the phase-averaged low repetition rate data of Wagner et al. [26]: (a) mode two, and (b) mode three**

bandpass filtered velocities where coherent structures were observed to rise and fall and undergo more rapid changes in size. For instance, the trajectory of structures in the downstream portion of the cavity (Fig. 7, $t = 0.37T_2$, e.g.) is consistent with upward undulation seen in the Fig. 13b. Similarly, the regions where wall-normal structures tend to rise more rapidly correspond to the upward undulations of PSD amplitude in Fig. 13b.

### E. Convective Velocities

Methodology

An example of waveforms corresponding to mode two bandpass filtered velocities ($v_{f2}$) is shown in Fig. 14a. The signals were obtained at $y = 0$ and were separated in $x$ by $0.9D$, which corresponds to a spacing of twenty vectors. The data in the figure are from the same time sequence as in Fig. 7 when mode two was clearly active. The cross correlation of the two signals is shown in Fig. 14b. Not surprisingly, the correlation between the two sinusoidal waveforms is quite strong. The maximum correlation occurs at a time delay $\tau$ of 213 μs, whereas the next highest peak occurs at a negative $\tau$.

Convective velocities are computed herein using the delay corresponding to maximum correlation and the known distance between measurement locations. In general, bandpass filtered velocity fields with active modes (Fig. 7 versus Fig. 8, e.g.) returned greater instances of positive convective velocities. This is depicted in Fig. 15, where histograms of mode two convective velocity ($U_{c2}$) obtained at a location of $x = 1.4D$ and $y = 0$ are shown. Convective velocities from all two hundred and forty five Mach 0.94 time sequences are shown in Fig. 15a, whereas only the forty percent most active modes are shown in the histogram on the right. As shown in Fig. 7 negative convective velocities for this location within the shear layer are nonphysical. The negative instances correspond to time sequences with lower modal amplitudes that returned weaker correlations. Negative convective velocities are not included in the bandpass filtered convective velocities. On the other hand, the subfigure on the right comprised of only active modes returns a much greater fraction of positive convective velocities. Thus, only active modes are considered in the subsequent convective velocity analysis.

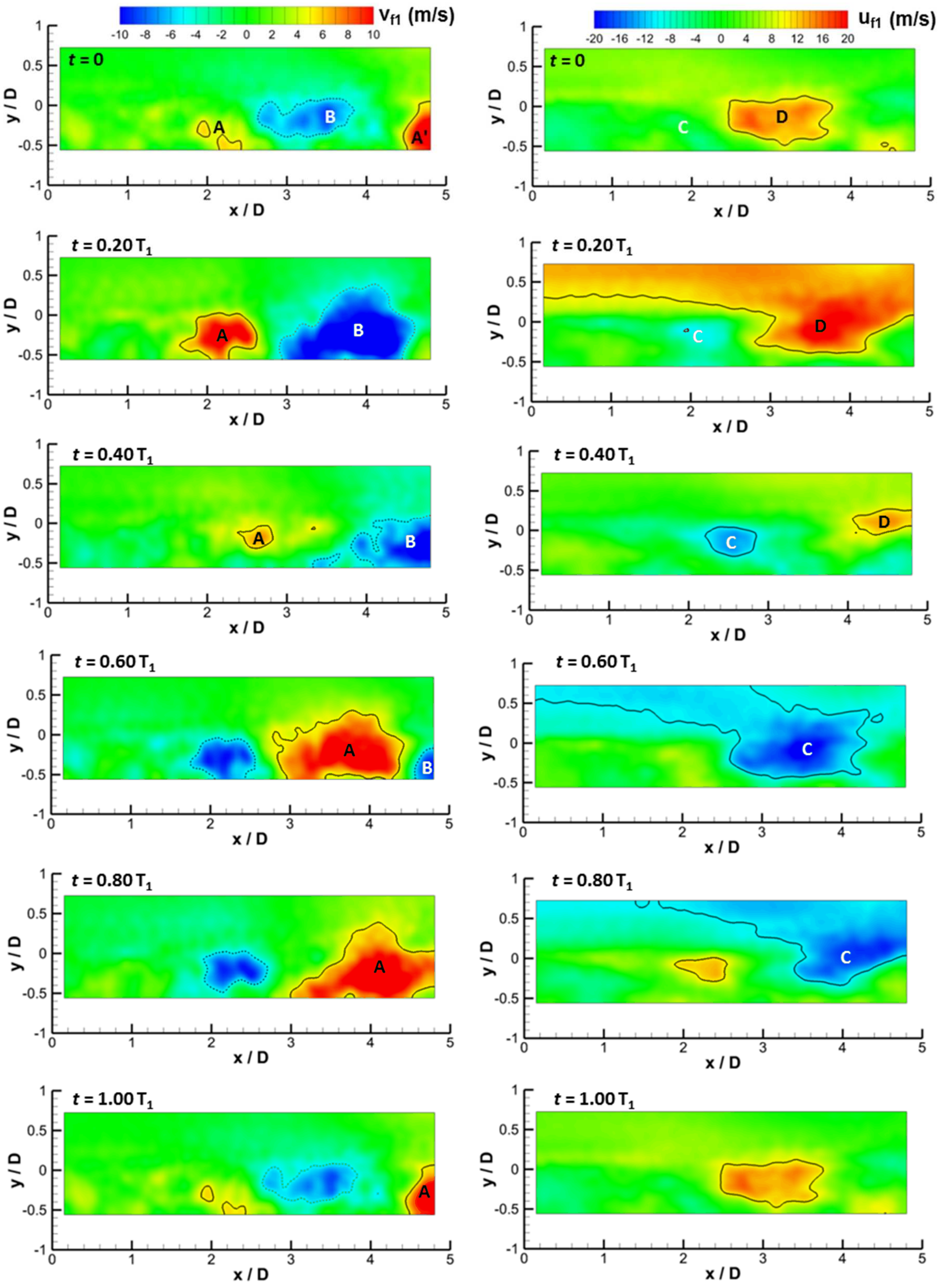

**Fig. 12** ***Mode one*** **bandpass filtered velocities: wall-normal (left), and streamwise (right). Solid lines correspond to 5 m/s and dashed lines correspond to -5 m/s in the wall-normal subfigures and 10 m/s and -10 m/s in the streamwise subfigures.**

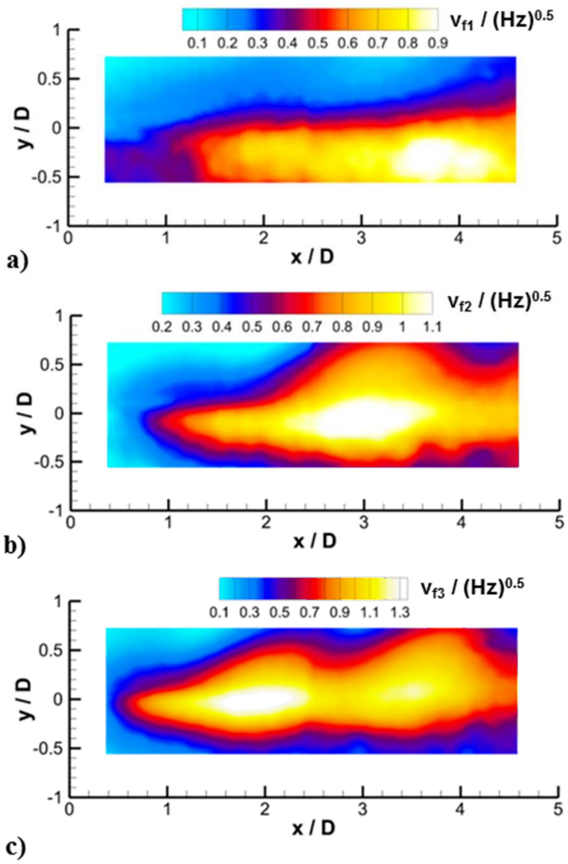

**Fig. 13 Spatial distributions of PSD amplitudes corresponding to cavity modes (a) one, (b) two, and (c) three**

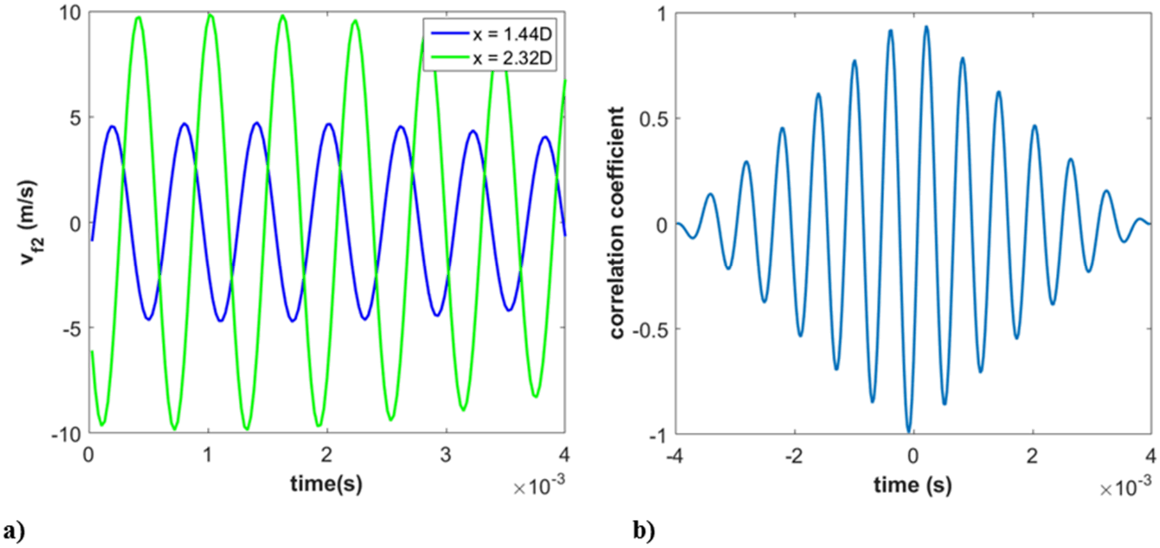

**Fig. 14 (a) Bandpass filtered velocities ($v_{f2}$) separated by a spacing of twenty of vectors and (b) cross correlation of the velocity waveforms.**

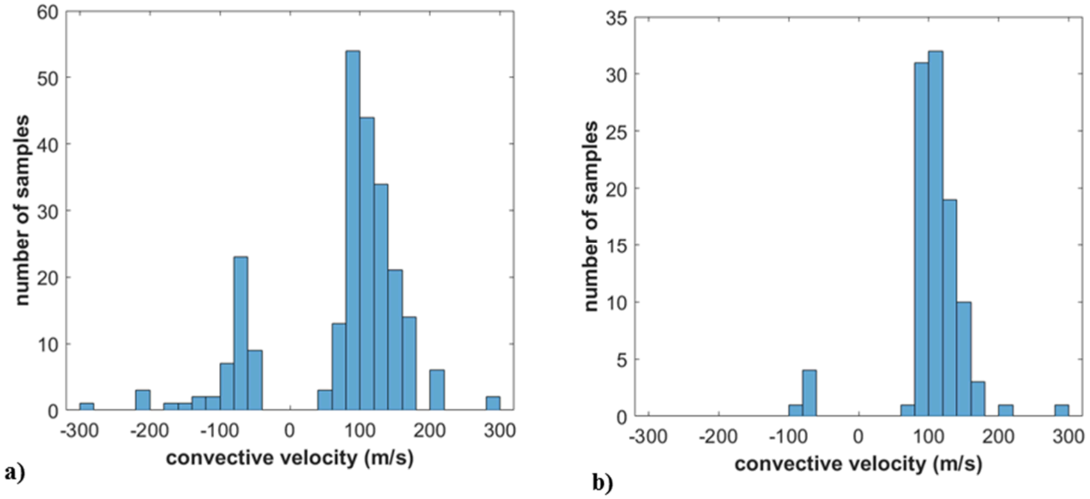

**Fig. 15 Histograms of mode 2 convective velocity: (a) velocities returned using all available samples, and (b) velocities using only the top forty percent most energetic time sequences**

Unfiltered Convective Velocities

The spatial distribution of convective velocity within the cavity for unfiltered data is displayed in Fig. 16a. The convection velocity is based on correlations of wall-normal velocity since $v$ it is more indicative of convection than the $u$ (Fig. 7, Fig. 9, Fig. 12 and [21]). $U_c$ at each location shown was found by computing the cross correlation between time series separated in $x$ by $0.9D$ (or twenty vector spacings). This methodology captures $U_c$ over the entire measurement domain, though the data are essentially smoothed by a moving average, lowpass filter. Similar results were obtained using a separation of ten and fifteen spacings.

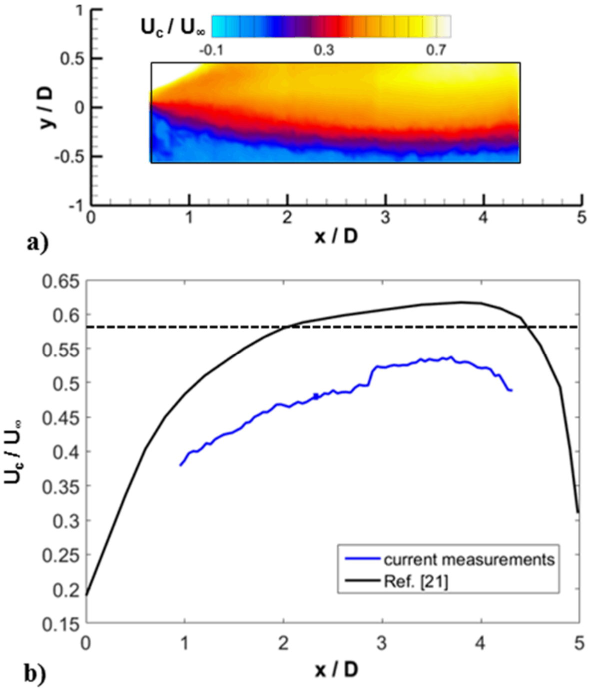

**Fig. 16 *Unfiltered* convective velocities based on the wall-normal component of raw velocity: (a) distribution within the cavity, and (b) centerline profile compared to the simulations of Larchevêque et al. [21].**

The unfiltered convective velocity figure demonstrates some expected trends. At a constant streamwise station, $U_c$ increases with $y$. Moreover, at constant $y$, the convective velocity gets larger with increasing streamwise distance. These trends are consistent with the mean flowfield (Fig. 2), which shows the shear layer dives downward into the cavity with streamwise distance. The convective velocity profile at a constant $y = 0$ is plotted in Fig. 16b. The uncertainty band corresponds to 95% confidence intervals of precision on the mean. $U_c$ increases as $x$ increases from $1D$ through $4D$. Over this same region, the slope of the profile decreases until a plateau region is reached between about $3D$ and $3.8D$. The convection velocity then begins to decrease for the rest of the measurement domain.

These measurements are consistent with previous cavity flow studies. Hassan [43], for example, measured similar convective velocities in incompressible cavity flows, including a region of decreasing slope, a plateau region, and a region of decreasing velocity following the plateau. The average convective velocities in Hassan [43] resided between about $0.40U_c$ and $0.50U_c$. In comparison, in the available measurement region, the average convective velocity here computes to $0.48U_\infty$, well below the $0.57U_\infty$ used in the Rossiter relation to correctly predict the tone frequencies (Fig. 3). The simulated convective velocity profile of Larchevêque [21], obtained at similar flow conditions to those herein, is also shown in Fig. 16. The current measurements show similar trends, although the simulated profile has an overall higher average convective velocity of $0.52U_\infty$. As discussed in Larchevêque [21], the relatively constant acceleration observed in the upstream portion of the cavity corresponds to a region where the flow is predominantly two dimensional, whereas the sudden decrease in the downstream portion is associated with the aft wall. The current measurement domain is not large enough to fully resolve these characteristics, although the regions with data do tend to demonstrate similar trends.

### Convective Velocities during Resonance

Convective velocities based on the bandpass filtered wall-normal velocities corresponding to cavity modes one, two, and three are shown in Fig. 17. The percentage of valid velocities at each measurement location is shown on the right side of the figure to show where the data are most reliable. A convective velocity was considered valid if it resided between 0 and $U_\infty$. In this section, the spacing between points used for cross correlation analysis was ten vectors. Spacings of fifteen and twenty vectors returned similar convective velocity distributions, though at mode three, the higher spacings were suffered from a higher percentage of invalid convective velocities, likely because of the smaller structures associated with mode three. The right hand side of the figure shows that the percentage of valid velocities measured in modes two and three is in most regions above 95%. On the other hand, mode one has a lower average valid velocity percentage of about 60%. Given this lower percentage, the mode one convective velocity distribution is treated as qualitative.

The convective velocities associated with the bandpass filtered vector fields present a unique view of resonance dynamics in cavity flows. Unlike like the measurements of unfiltered velocity data shown here (Fig. 16) and those presented in other studies [21, 43], a periodicity is observed in the velocities associated with the cavity tones. There appears to be a wavelength in the convective velocity, which decreases with increasing mode number in a fashion analogous to the spatial wavelength (Fig. 11). To explain this observation, lines of constant PSD amplitude taken from Fig. 13 are also shown in the convective velocity figures. In general, the convective velocity increases in regions where the modal PSD amplitude increases. As previously discussed, undulations in the PSD amplitude are associated with upward and downward motions of coherent flow structures. Therefore, the increases in convective velocity seen in Fig. 17 are likely the result of the coherent structures propagating upward to a higher portion of the shear layer where the mean convective is higher (Fig. 2a). Likewise, when the coherent regions move downward, they move to a region of locally lower mean velocity where the convective velocity should be lower. Similar trends were observed in convective velocities given from cross correlations of filtered streamwise velocities, namely a decreasing wavelength in the convective velocity fields was observed as the cavity mode number increased.

Convective velocity profiles obtained at $y = 0$ for all three cavity modes are plotted in Fig. 18. On average, the convective velocity increases with cavity mode number. Specifically, the average $U_c$ of modes one, two, and three in the figure calculates to $0.26U_\infty$, $0.43U_\infty$, and $0.48U_\infty$, respectively. This likely related to the fact that as the cavity mode number increases, more energy tends to reside at higher locations within the flowfield (Fig. 13) where the local velocity is higher. Like the unfiltered convective, there is an overall increase in mode three velocity with $x$. Such an overall increase is not seen in the mode two profile, though this may be masked by sample dropout in the upstream portion of the measurement region. Finally, Fig. 18 reemphasizes the periodicity of the convective velocity associated with the cavity resonance. The wavelengths observed in the convective velocity resemble those seen in the bandpass wall-normal velocities (Fig. 11) and are consistent with the PSD amplitude distributions of Fig. 13.

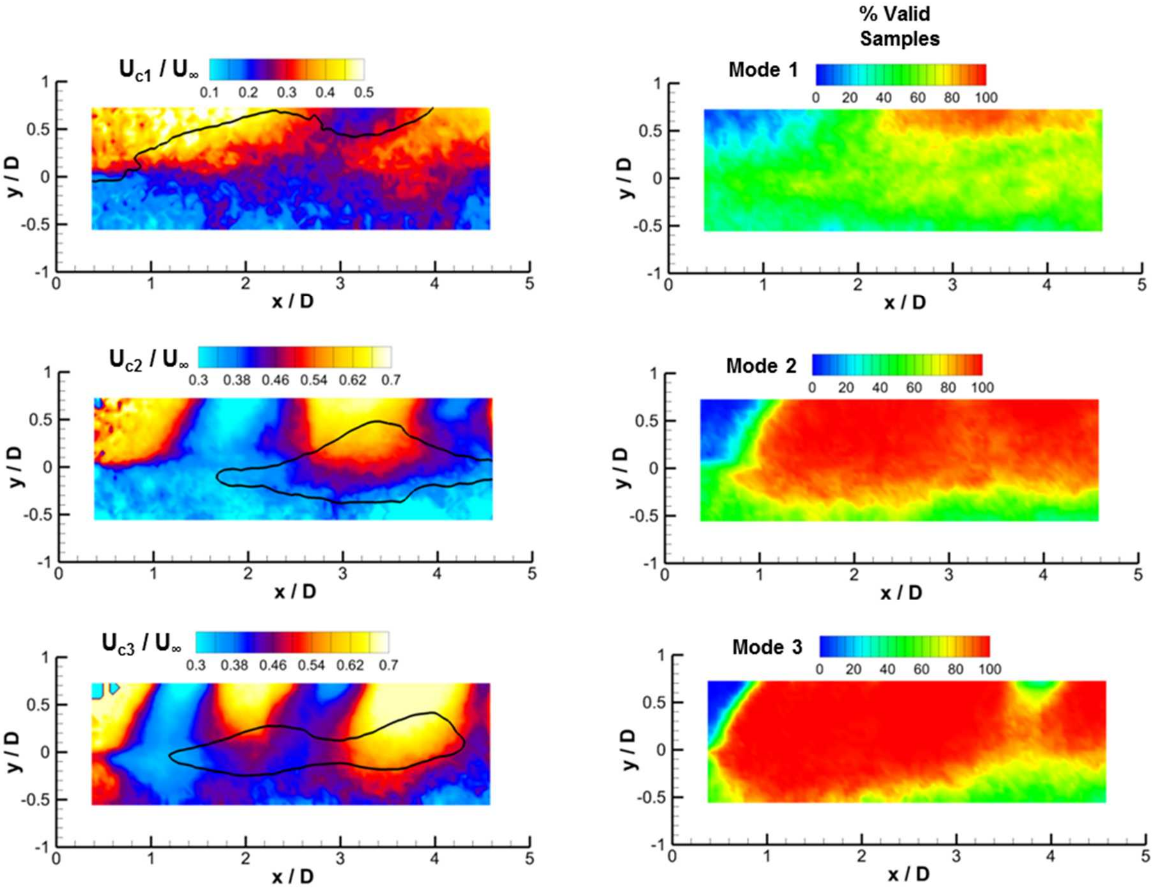

**Fig. 17** *Modal convective velocities* **based on the wall-normal component of filtered velocity of modes 1 – 3 (left), and percentage of valid velocities returned at each measurement location (right). The black lines in the convective velocity figures correspond to regions of constant modal PSD amplitude taken from Fig. 13 of 0.2 (mode 1), 0.85 (mode 2), and 1 (mode 3).**

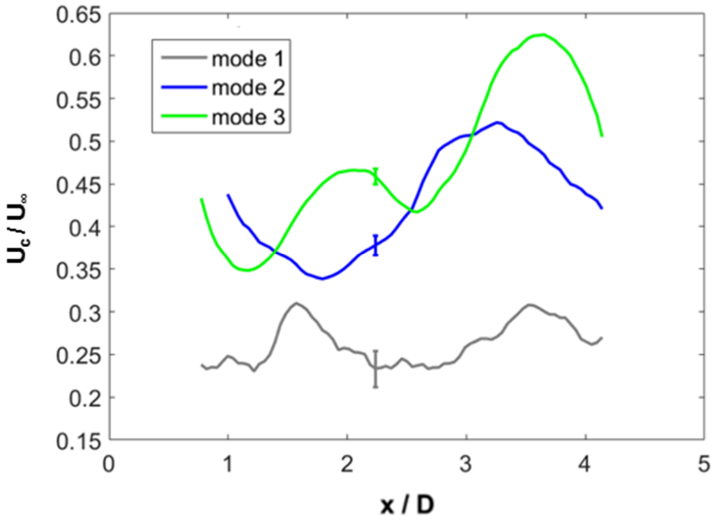

**Fig. 18** *Modal convective velocities* **based on the wall-normal filtered velocities of modes 1 – 3 at** ***y*** **= 0**

## IV. Conclusions

The Mach 0.94 flow over a cavity having a length-to-depth ratio of five was explored using TR-PIV with a pulse-burst laser. The incoming boundary layer was turbulent with a 99% boundary layer thickness equal to about half the cavity depth.

Convective velocities were computed using cross correlations of vertical velocity. In the raw (unfiltered) data, the convective velocity measured in the shear layer increased with streamwise distance in a fashion similar to other studies.

The TR-PIV data were used to probe the resonance dynamics of the first three cavity (Rossiter) tones. Bandpass filtering was employed to reveal the coherent flow structure associated with each tone. The first Rossiter mode was associated with a propagation of large scale structures in the recirculation region, while the second and third modes contained organized structures consistent with convecting vortical disturbances. The wavelengths of the second and third modes were quite similar to those observed in a previous study by the current authors using low repetition rate PIV, which was phase averaged using bandpassed high-speed pressure data.

Spatial distributions of PSD amplitudes were utilized aid understanding of the resonance dynamics. Like the bandpass filtered velocity fields, the PSD distributions associated with resonance were observed to exhibit a periodicity. Moreover, the PSDs showed that the modal energy tended to reside lower in the cavity for lower cavity mode numbers, an observation also consistent with the bandpassed velocity fields.

Convective velocities of the cavity tones were also computed using two point correlations of the bandpass filtered velocity. The convective velocities were found to decrease with mode number, an observation consistent with the modal activity residing in lower portions of the cavity in regions of lower local mean velocities.

The convective velocity fields associated with resonance were found to have wavelengths that decreased with increasing mode number. Such oscillations were hypothesized to be associated with wall-normal motions of coherent structures during resonance.

## Acknowledgments

The authors would like to acknowledge Dr. Edward DeMauro and Dr. Matthew Barone for very valuable discussions on coherent structures in turbulence and on cavity flows. Wavelet software was provided by C. Torrence and G. Compo, and is available at URL: http://paos.colorado.edu/research/wavelets/.

## References

[1] Rossiter, J. E., "Wind-Tunnel Experiments on the Flow Over Rectangular Cavities at Subsonic and Transonic Speeds," Aeronautical Research Council Reports and Memoranda, October 1964.

[2] Wagner, J. L., Casper, K. M., Beresh, S. J., Hunter, P. S., Spillers, R. W., Henfling, J. F., and Mayes, R. L., "Fluid-structure interactions in compressible cavity flows," *Physics of Fluids*, Vol. 26, No. 6, pp.066102.

[3] Barone, M., and Arunajatesan, S., "Pressure loading within rectangular cavities with and without a captive store," AIAA Paper 2014-1406.

[4] Arunajatesan, S., Ross, M., Barone, M., and Garret, T. J., "Validation of an FSI Modeling Framework for Internal Captive Carriage Applications," AIAA Paper 2013-2157.

[5] Wagner, J. L., Casper, K. M., Beresh, S. J., Hunter, P. S., Spillers, R. W., and Henfling, J. F., "Response of a Store with Tunable Natural Frequencies in Compressible Cavity Flow," *accepted for publication in AIAA Journal*, also AIAA Paper 2015-1293.

[6] Rockwell, D., and Naudascher, E., "Self-sustained oscillations of impinging free shear layers," *Annual Review of Fluid Mechanics*, Vol. 11, 1979, pp. 67-94.

[7] Rockwell, D., and Naudascher, E., "Review-Self Sustaining Oscillations of Flow Past Cavities," *Journal of Fluids Engineering*, Vol. 100, 1978, pp. 152-165.

[8] Rowley, C. W., and Williams, D. R., "Dynamics and Control of High-Reynolds-Number Flow over Open Cavities," *Annual Review of Fluid Mechanics*, Vol. 38, 2006, pp. 251-276.

[9] Cattafesta, L. N., Song, Q., Williams D. R., Rowley C. W., and Alvi, F. S., "Active control of flow-induced cavity oscillations," *Progress in Aerospace Sciences*, Vol. 44, 2008, pp. 479-502.

[10] Tracy, M. B., and Plentovich, E. B., "Cavity Unsteady-Pressure Measurements at Subsonic and Transonic Speeds," NASA Technical Paper 3669, December 1997.

[11] Beresh, S. J., Wagner, J. L., Pruett, B. O., Henfling, J. F., and Spillers, R. W., "Supersonic Flow over a Finite-Width Rectangular Cavity," *AIAA Journal*, Vol. 53, No. 2, 2014, pp. 296-310.

[12] Beresh, S. J., Wagner, J. L., Henfling, J. F., Spillers, R. W., and Pruett, B. O., "Width Effects in Transonic Flow over a Rectangular Cavity," *AIAA Journal*, Vol. 53, No. 12, 2015, pp. 23831-3835.

[13] Arunajatesan, S., Barone, M. F., Wagner, J. L., Casper, K. M., and Beresh, S. J., "Joint experimental/computational investigation into the effects of finite width on transonic cavity flow," AIAA Paper 2014-3027.

[14] Casper, K. M., Wagner, J. L., Beresh, S. J., Henfling, J. F., Spillers, R. W., & Pruett, B. O., "Complex Geometry Effects on Cavity Resonance," *accepted for publication in AIAA Journal*, also AIAA Paper 2015-1291.

[15] Ukeiley, L., Sheehan, M., Coiffet, F., Alvi, F., Arunajatesan, S., and Jansen, B., "Control of pressure loads in geometrically complex cavities," *Journal of Aircraft*, Vol. 45, No. 3, 2015, pp.1014-1024.

[16] DeMauro, E. P., Beresh, S. J., Wagner, J. L., Henfling, J. F., and Spillers, R. W., "Volumetric Measurement of Transonic Cavity Flow Using Stereoscopic Particle Image Velocimetry," to be presented at the 53rd AIAA Aerospace Sciences Meeting, January 2015.

[17] Krishnamurty K., "Acoustic radiation from two-dimensional rectangular cutouts in aerodynamic surfaces," NACA TN 3487, 1955.

[18] Sarohia, V., "Experimental investigation of oscillations in flows over shallow cavities," *AIAA Journal*, Vol. 15, No. 7, 1977, pp. 984-990.

[19] Kegerise, M. A., "An Experimental Investigation of Flow Induced Cavity Oscillations," Ph.D. Thesis, Department of Mechanical Engineering, Syracuse University, New York, USA, 1999.

[20] Kegerise, M. A., Spina, E. F., Garg, S., Cattafesta, L. N., "Mode-Switching and Nonlinear Effects in Compressible Flow Over a Cavity," *Physics of Fluids*, Vol. 16, No. 3, 2005, pp. 678-687.

[21] Larchevêque, L., Sagaut, P., Lê, T. P., and Compte, P., "Large-eddy simulation of a compressible flow in a three-dimensional open cavity at high Reynolds number," *Journal of Fluid Mechanics*, Vol. 516, 2004, pp. 265-301.

[22] Brès, G. A., and Colonius, T., "Three-Dimensional Instabilities in Compressible Flow over Open Cavities," *Journal of Fluid Mechanics*, Vol. 599, 2008, pp. 309-339.

[23] Casper, K. M., and Arunajatesan, S., "Modal Decomposition of Pressure Data in Cavity Flows," AIAA Paper 2015-2938.

[24] Murray, N. E., and Ukeiley, L. S., "Modified quadratic stochastic estimation of resonating subsonic cavity flow," *Journal of Turbulence*, Vol. 8, No. 53, 2007, pp. 1-22.

[25] Murray, N., Raspet, R., & Ukeiley, L., "Contributions of turbulence to subsonic cavity flow wall pressures," *Physics of* Fluids, Vol. 23, No. 1, 2011, pp. 015104.

[26] Wagner, J. L., Casper, K. M., Beresh, S. J., Arunajatesan, S., Henfling, J. F., Spillers R. W., Pruett, B. O., "Relationship between Acoustic Tones and Flow Structure in Transonic Cavity Flow," AIAA Paper 2015-2937.

[27] Hussain, A. K. M., "Coherent Structures and Turbulence," *Journal of Fluid Mechanics*, vol. 173, pp. 303-356, 1986.

[28] Song, Q., Closed-Loop Control of Flow-Induced Cavity Oscillations, Ph.D. Thesis, Department of Mechanical and Aerospace Engineering, University of Florida, Gainesville, USA, 2008.

[29] Murray, N. E., Sallstrom, E., and Ukeiley, L., "Properties of Subsonic Open Cavity Flow Fields," *Physics of Fluids*, Vol. 21, No. 9, 2009.

[30] Wagner, J. L., Casper, K. M., Beresh, S. J., Pruett, B. O., Spillers R. W., and Henfling, J. F., "Mitigation of Wind Tunnel Wall Interactions in Subsonic Cavity Flows," *Experiments in Fluids*, Vol. 56, 2015.

[31] Shaikh, F. N. and Gaster, M., "The Non-Linear Evolution of Modulated Waves in a Boundary Layer*," Journal of Engineering Mathematics*, Vol. 28, 1994, pp. 55–71.

[32] Jordan, D., Miksad, R. W., and Powers, E. J., "Implementation of the Continuous Wavelet Transform for Digital Time Series Analysis," Review of Scientific Instruments, Vol. 68, No. 3, March 1997, pp. 1484–1494.

[33] Torrence, C. and Compo, G. P., "A Practical Guide to Wavelet Analysis," *Bulletin of the American Meteorological Society*, Vol. 79, No. 1, 1998, pp. 61–78.

[34] Samimy, M., and Lele, S. K., "Motion of Particles with Inertia in a Compressible Free Shear Layer," *Physics of Fluids A*, Vol. 3, No. 8, 1991, pp. 1915-1923.

[35] Slipchenko, M. N., Miller, J. D., Roy, S., Gord, J. R., Danczyk, S. A., and Meyer, T. R., "Quasi-Continuous Burst-Mode Laser for High-Speed Planar Imaging," *Optics Letters*, Vol. 37, No. 8, pp. 1346-1348, 2012.

[36] Slipchenko, M. N., Miller, J. D., Roy, S., Gord, J. R., and Meyer, T. R., "All-Diode-Pumped Quasi-Continuous Burst-Mode Laser for Extended High-Speed Planar Imaging," *Optics Express*, Vol. 21, No. 1, pp. 681-689, 2013.

[37] Beresh, S. J., Kearney, S. P., Wagner, J. L., Guildenbecher, D. R., Henfling, J. F., Spillers, R. W., Pruett, B. O., Jiang, N., Slipchenko, M., Mance, J., and Roy, S., "Pulse-Burst PIV in a High-Speed Wind Tunnel," *Measurement Science and Technology*, Vol. 26, No. 9, 2015.

[38] Russell, D., "Electronic Supplement to Development of a Time-Domain, Variable-Period Surface Wave Magnitude Procedure for Application at Regional and Teleseismic Distances, Part I: Theory," *Bulletin of the Seismological Society of America*, 2006, URL: http://www.seismosoc.org/publications/BSSA_html/bssa_96-2/05055-esupp/.

[39] Heller, H. H., and Bliss, D. B., "The Physical Mechanism of Flow Induced Pressure Fluctuations in Cavities and Concepts for Suppression," AIAA Paper 75-491.

[40] Seena, A., Sung, H. J., "Spatiotemporal representation of the dynamic modes in turbulent cavity flows," *International Journal of Heat and Fluid Flow*, Vol. 4, 2013, pp. 1-13.

[41] Lee, S. B., Seena, A., Sung, H. J., "Self-sustained oscillations of turbulent flow in an open cavity," *Journal of Aircraft*, Vol. 47, No. 3, 2010, pp. 820-834.

[42] Li, W., Nonomura, T.,Fujii, K., "On the feedback mechanism in supersonic cavity flows," *Physics of Fluids*, Vol. 25, No. 5, 2013, pp. 056101.

[43] Hassan, M., Labraga, L., Keirsbulck, L., "Aero-acoustic oscillations inside large deep cavities," 16th Australasian Fluid Mechanics Conference (AFMC), School of Engineering, The University of Queensland, 2007, pp. 421-428.